



## Influence of welding on low cycle fatigue properties of Co-based superalloy FSX-414

Kh. RAHMANI, A. TORABIAN

Energy and Mechanical Engineering Department, Abbaspour College of Engineering,  
Shahid Beheshti University, P. O. Box 16765-1719, Tehran, Iran

Received 25 May 2015; accepted 17 March 2016

**Abstract:** Co-based superalloys such as FSX-414 have been recently used in gas turbine first stage nozzles. During service, nozzles are exposed to low cycle fatigue, which can lead to cracking of these components. The cracks on these nozzles are usually welded with tungsten arc welding (TIG) using Co-based filler metals. In this paper, the effect of TIG on the tensile and low cycle fatigue properties of Co-based superalloy FSX-414 was studied at 950 °C. The experimental results show that the yield and ultimate tensile stresses of welded and unwelded specimens are comparable to each other. But toughness of welded specimens is lower than that of unwelded ones. The low cycle fatigue properties of FSX-414 were studied at a strain rate of  $3.3 \times 10^{-4} \text{ s}^{-1}$ , strain ratio  $R=-1$  ( $R=\epsilon_{\min}/\epsilon_{\max}$ ) and  $\Delta\epsilon_t$  (total strain change) from 0.8% to 2%. In welded specimens, at high strain cycling, the nucleation and growth of cracks occur in the welded zone. But at  $\Delta\epsilon_t=0.8\%$ , fracture occurs in the same zones of unwelded specimens. The results show that the total fatigue lives of the welded specimens are shorter than those of unwelded ones. In all of the low cycle fatigue tests, softening phenomena are observed.

**Key words:** Co-based superalloy; tensile property; low cycle fatigue; welding

### 1 Introduction

Gas turbine hot path components, in particular the first stage nozzles, undergo complex thermal and mechanical stresses during start-up and shut down. Co-based superalloy such as FSX-414 is the best choice to utilize in the first stage nozzle due to good stress-rupture, excellent hot corrosion and oxidation properties, good weldability and high structure stability [1–5]. However, extensive cracking has been observed especially around the leading, trailing edges and between the airfoils [5,6]. To extend lifetime of these nozzles, the large and deep cracks are welded and repaired. Several welding technologies can be used for repairing, including gas tungsten arc welding (TIG), electron beam welding (EBW), activated diffusion healing (ADH), liquid phase diffusion sintering (LPDS), transient liquid phase (TLP) and laser beam welding (LBW) [7–14]. TIG welding is a process that is well suited for the repair of thin sections of nozzles because the heat input is highly localized and controllable. The localized heat used to join materials is produced by

passing an electric current through a non-consumable electrode made of tungsten or tungsten alloy, into the work piece [7]. EBW process was chosen because it produces a weld cross-section with a high depth-to-width ratio, which means that full penetration welds in thick sections could be made in a single pass and with minimal heat input. In most cases filler alloys are not required, which simplifies the metallurgical evaluation of interactions between the weldment and base alloy [8]. ADH was originally developed by GE's Aircraft Engine Group for vane (nozzle) repair. GE Power Systems' Inspection and Repair Services (I&RS) has modified the process for use with heavy duty industrial gas turbine alloys. The ADH process uses a mixture of superalloy powders and an organic binder tailored to meet the part's specific design requirements [9,10]. LPDS uses a combination of a high melting point powder (typically a composition similar to the superalloy being joined) and a low melting point powder (typically a braze with boron as the melting point depressant). The powders are applied to the area to be repaired in the form of a paste, putty, or sintered perform. The repair is subsequently sintered in vacuum furnace below the melting point of

the base metal substrate. LPDS process was used to restore wall thickness on the concave and convex surfaces of the airfoil, repair cracks, pits dents and build up the hook fit areas as a result of downstream deflection of the inner buttress seal areas, as a result axial creep [10]. TLP bonding is a relatively new bonding process that joins materials using an interlayer. On heating, the interlayer melts and the interlayer element (or a constituent of an alloy interlayer) diffuse into the substrate materials, causing isothermal solidification. The result of this process is a bond that has a higher melting point than the bonding temperature. This bonding process has found many applications, most notably the joining and repair of Co-based superalloy components [11–13]. LBW uses a concentrated and columnar beam of light to produce heat in the weld joint. The light beam consists of a stream of photons which are focused by lenses and mirrors to small spot sizes in order to create the high power density required. The condition of the surface of the work piece, especially reflectivity, has a significant effect on the weldability because LBW relies on light beams for heating. The small spot size of LBW makes it generally unsuitable for wide gap [13]. Among the welding techniques, the gas tungsten arc welding (GTAW or TIG) process is widely used for surface crack repair of the nozzles, due to its lower facility cost [8,12,15,16]. Commercial filler alloy L-605 is selected for TIG welding FSX-414 [8]. One of the limitations of this welding technique is incomplete or insufficient penetration of melts in the root of V-type cracks [15]. Therefore, V-type cracks must be converted to U-type ones, welding parameter should be improved and/or the welding technique should be changed. In this work, the effect of insufficient penetration of melts on the low cycle fatigue of Co-based superalloy was studied.

The fabric and repaired nozzles were exposed to cyclic loading at high temperatures. This problem is often simulated in laboratory as LCF. There have been a few reports on LCF of Co-based superalloy FSX-414 [17–24]. However, there are few references in the field of influence of welding on the mechanical properties of FSX-414.

## 2 Experimental

An investment air casting method was used so that adequate amount of round bars (50 bars) can be obtained. The chemical composition of the material, FSX-414,

which was determined by WAS Foundry-Master spectrometer is given in Table 1. A number of the round bars (24 bars) were solution-treated at 1150 °C for 4 h, machined and age-treated at 980 °C for 4 h [8,12,25]. Other specimens were solution-treated (pre-weld heat treatment), machined, grooved in the center of gauge length (V-type with 60°) and welded by TIG. The filler metal used for welding was L-605. The largest width of cracks found on nozzles was about 1.5 mm [26]. Therefore, for the process qualification, the mechanical properties tests (tensile and LCF) were undertaken on specimens with a joint gap of 1.5 mm. After welding, the specimens were solution-treated. After solution treatment, cylindrical test specimens were aged and machined out to bring them as instructed by ASTM-E 8 and ASTM-E 606, as shown in Fig. 1. To make sure that there are no cracks, all specimens were inspected by dye penetration test. The chemical weld metal is shown in Table 1. Tensile tests for unwelded and welded specimens were performed at 950 °C and constant strain rate of  $8.3 \times 10^{-4} \text{ s}^{-1}$ . All of the tensile tests were performed according to standard ASTM-E 21. The LCF tests were performed on both the unwelded and welded specimens under triangular wave form cyclic strain,  $R = \epsilon_{\min}/\epsilon_{\max} = -1$ ;  $\Delta\epsilon_t$  values of 0.8%, 1.2%, 1.6%, 2%; 950 °C and strain rate of  $3.3 \times 10^{-4} \text{ s}^{-1}$ . In order to minimize the effect of surface roughness on LCF results, the surfaces of all the specimens were polished according to ASTM-E 606 after aging heat treatment. The specimens were gripped by threaded jaws to the modified electromechanical testing machine (Instron model 6027). The specimens were brought to testing temperature in a cylindrical electric resistance Instron furnace (model SF375) with an accuracy of  $\pm 1$  °C. To control the temperature, a R-type thermocouple was attached on the specimen within the gauge length region. To record the magnitudes and variations of the cyclic strains applied on specimens, a linear variable differential transformer (LVDT) leg type extensometer was used. Figure 1 illustrates the specimen dimension and the extensometer position on a specimen. The microstructures of specimens were studied by SEM (model Vega Tscan Philips).

## 3 Results and discussion

The microstructures of unwelded and welded specimens are shown in Figs. 2 and 3, respectively. The microstructure of FSX-414 consists of  $\alpha$ -Co phase

**Table 1** Chemical compositions of FSX-414 and filler metal L-605 (mass fraction, %)

Specimen	Cr	Ni	W	Fe	Si	Mn	C	B	Co
FSX-414	29.64	10.37	7.04	0.92	0.72	0.689	0.274	0.007	Bal.
L-605	24.5	11.42	11.8	1.5	1	1.7	0.1	–	Bal.

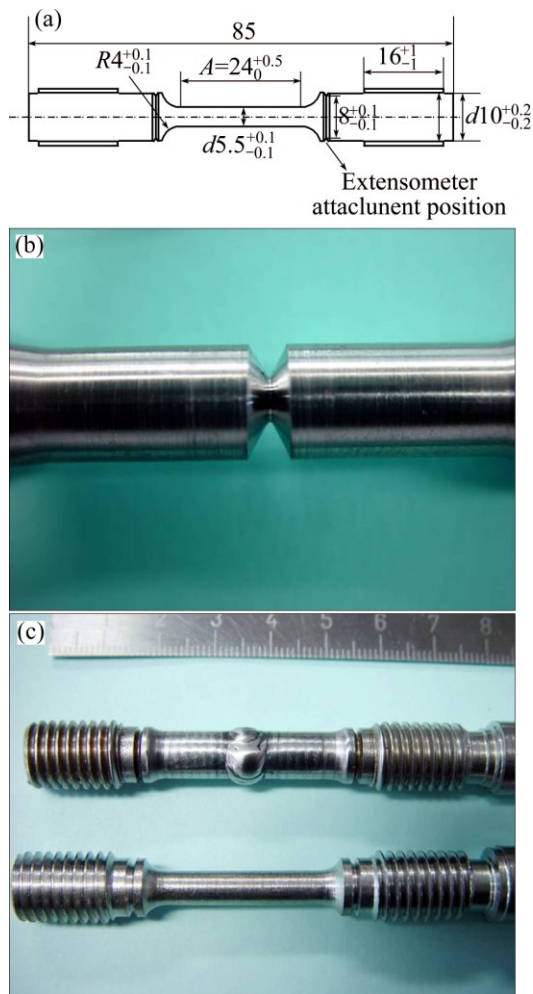


**Fig. 1** Tensile and fatigue specimen dimensions (mm) according to ASTM-E 8 and ASTM-E 606 (a), grooved specimen (b) and welded specimens before and after machining (c)

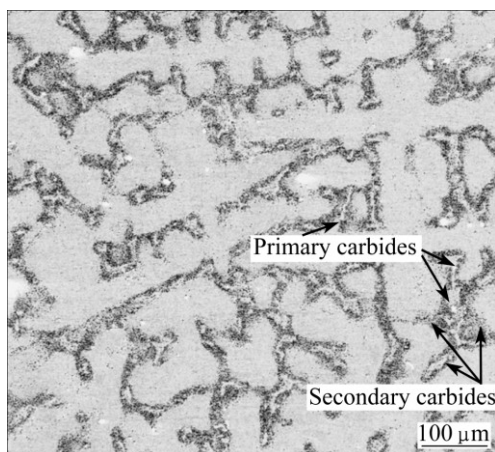


**Fig. 2** Microstructure of FSX-414 (unwelded specimen) consisting of primary and secondary carbides

matrix, primary and secondary carbides. The carbides contribute significantly to strengthening. They precipitate at grain boundaries and in interdendritic regions. During aging heat treatment or during service at

high temperatures, secondary carbides, usually  $M_{23}C_6$  ( $M=Co, Cr, W$  and  $Ni$ ), precipitate from primary carbides [3,6]. The carbide network at or near grain boundaries prevents grain boundary sliding and provides strengthening in the alloy. Carbides also play an important role in grain boundary oxidation resistance. Figure 3 shows the microstructures of the specimen after welding, solution and aging treatment. The weld region consists of  $\alpha$ -Cr matrix. In L-605 weld metal microstructure, there is no network carbide. The microstructures of FSX-414 and welded metal consist of 70–80  $\mu m$  and 30–40  $\mu m$  grain size, respectively. The grain size was determined by the linear intercept method according to ASTM-E 112. The average tensile test results at 950  $^{\circ}C$  are shown in Table 2. The stress–elongation curves for comparison of tensile behavior of welded and unwelded specimens are shown in Fig. 4.

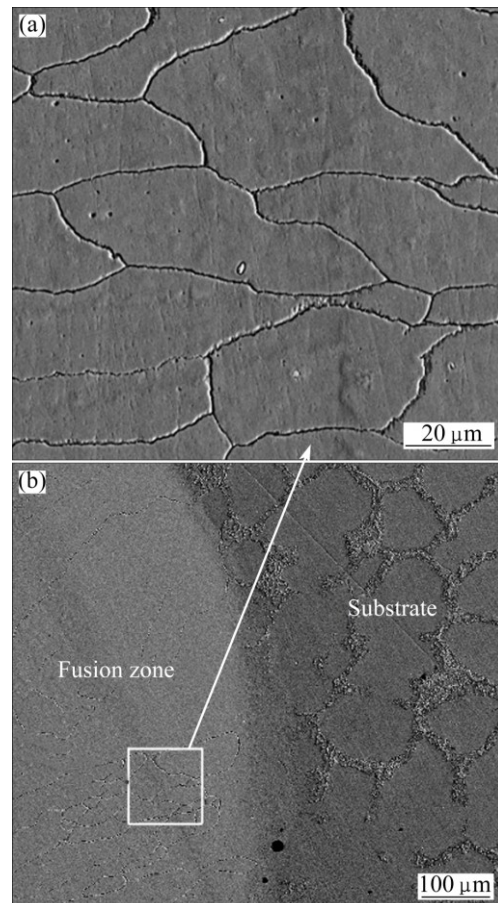


**Fig. 3** Microstructures of welded specimen (fusion zone grains are oriented essentially perpendicular to substrate-fusion zone interface)

**Table 2** Average tensile results for unwelded and welded FSX-414 at 950  $^{\circ}C$

Specimen	$\sigma_u/MPa$	$\sigma_y/MPa$	El/%	Elasticity/MPa
Unwelded	119.5	94.3	52	9450
Welded	122	95	25	9320

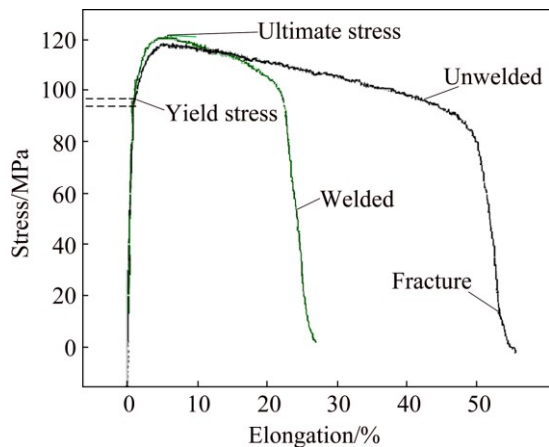


**Fig. 4** Stress–elongation curves of unwelded and welded specimens

Experimental tensile results show that the yield and ultimate stresses of unwelded and welded specimens are relatively equal. But toughness (the area under the stress–elongation curve), reductions in area and elongation of the welded specimen are lower than those of unwelded specimens. It is assumed that the low ductility values measured (welded specimen) during this tensile test are related to microstructure, the presence of defects and discontinuity (due to insufficient penetration of melts) in weld joint [8]. The fusion zone grains are oriented essentially perpendicular to the substrate–fusion zone interface (Fig. 3). The fracture surfaces of the unwelded and welded specimens are shown in Figs. 5 and 6, respectively. Comparing Fig. 5 with Fig. 6 shows that the microvoid number in the unwelded specimen is more than that in the welded specimen. The fracture surface of the welded specimen tensed and fractured is shown in Fig. 6, in which cleavage surfaces due to the brittle fracture are clearly observed.

The results of LCF tests of unwelded and welded specimens at  $\Delta\epsilon_f$  values of 0.8%, 1.2%, 1.6%, 2% are

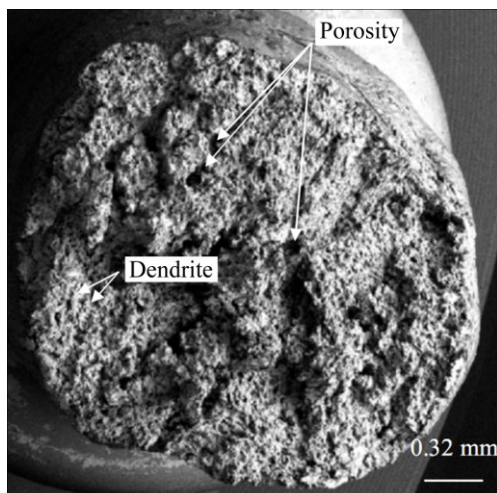


**Fig. 5** Fracture surface of unwelded specimen after tensile test

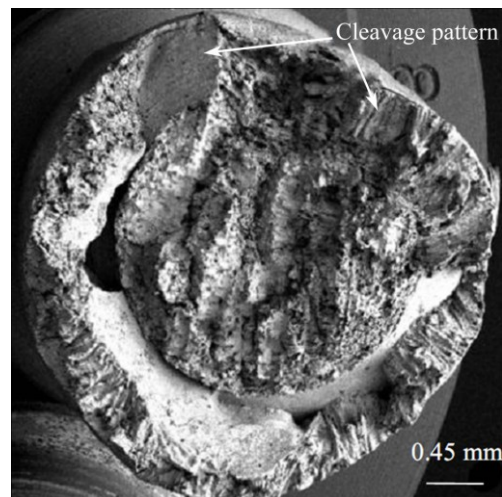


**Fig. 6** Fracture surface of welded specimen after tensile test

listed in Table 3. Figures 7 and 8 present stress–strain hysteresis loops and Figs. 9 and 10 show the cyclic stress response with time respectively. During the fatigue process in the low cycle fatigue, the stress–strain hysteresis curves change gradually. The deformation of the gage length was measured by displacement gage with leg type extensometer attached. Since the maximum and the minimum strains were controlled, the peak stresses at positive and negative loads were changeable. For example, in the case of  $\Delta\epsilon_f=0.8\%$ , the maximum and the minimum strains of  $\pm 0.4\%$  were controlled. Fatigue life decreases with increasing strain amplitude. At  $R=-1$ , the cyclic stress amplitude decreases during cyclic deformation. This phenomenon is called softening. In strain controlled tests shown in Figs. 9 and 10, softening phenomenon, steady-state, crack initiation and final fracture are observed. The investigation results on the LCF fatigue behavior of other materials indicate that the softening has been identified with 1) shearing of precipitates by gliding dislocation, 2) dissolution of precipitates and 3) disordering of precipitates [22]. The

**Table 3** Average LCF results for unwelded and welded FSX-414 at 950 °C

Specimen	$\Delta\epsilon_f/\%$	$\sigma_{max}$ (at cycle 1)/ MPa	$\sigma_{min}$ (at cycle 1)/ MPa	$\Delta\sigma/2$ (at cycle 1)/ MPa	$N_i$	$N_f$
Unwelded	0.8	140	-110	125	513	638
	1.2	110	-180	145	144	195
	1.6	180	-160	170	81	102
	2	170	-200	185	38	50
Welded	0.8	160	-180	170	268	346
	1.2	170	-180	175	72	89
	1.6	170	-190	180	42	45
	2	180	-200	190	20	22

$N_i$  is number of cycles to crack initiation;  $N_f$  is number of cycles to failure

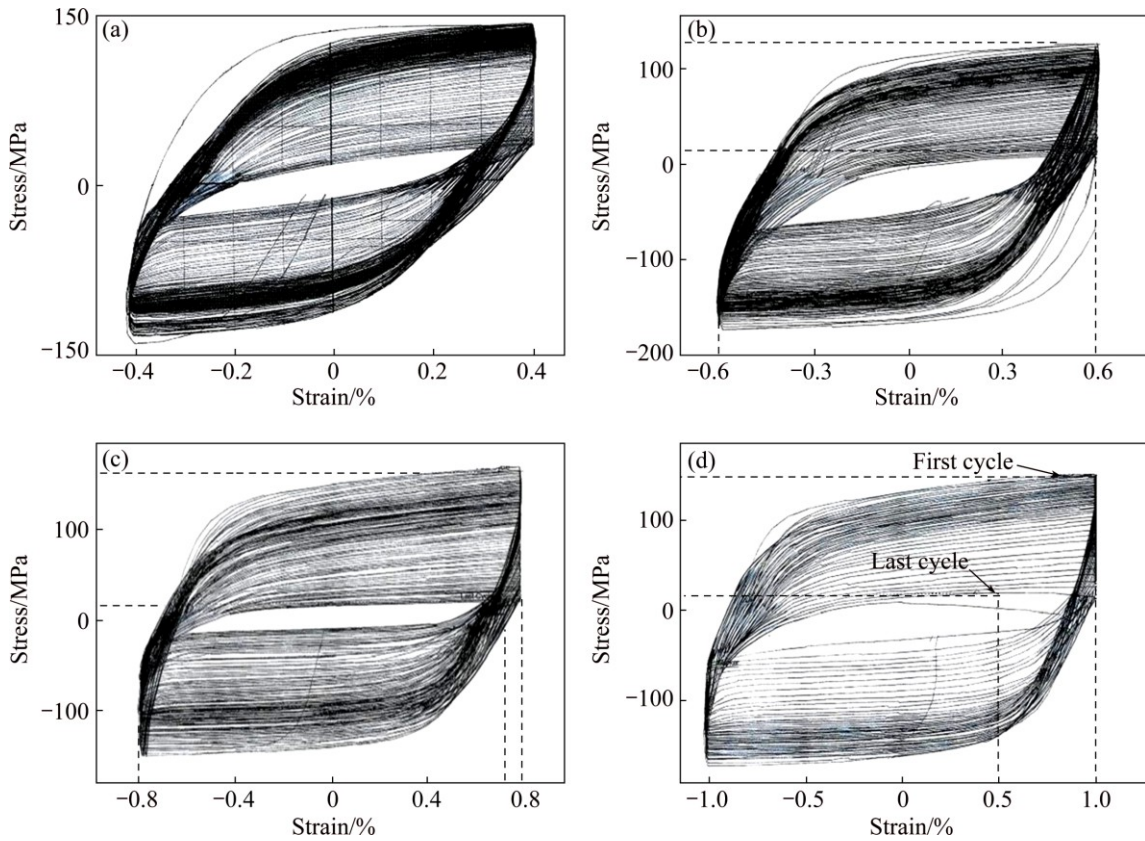


**Fig. 7** Stress–strain hysteresis loops obtained for unwelded specimen under LCF at  $\Delta\epsilon_t$  values of 0.8%–2%, 950 °C,  $R=-1$  and strain rate of  $3.3 \times 10^{-4} \text{ s}^{-1}$ : (a)  $\Delta\epsilon_t=0.8\%$ ; (b)  $\Delta\epsilon_t=1.2\%$ ; (c)  $\Delta\epsilon_t=1.6\%$ ; (d)  $\Delta\epsilon_t=2\%$

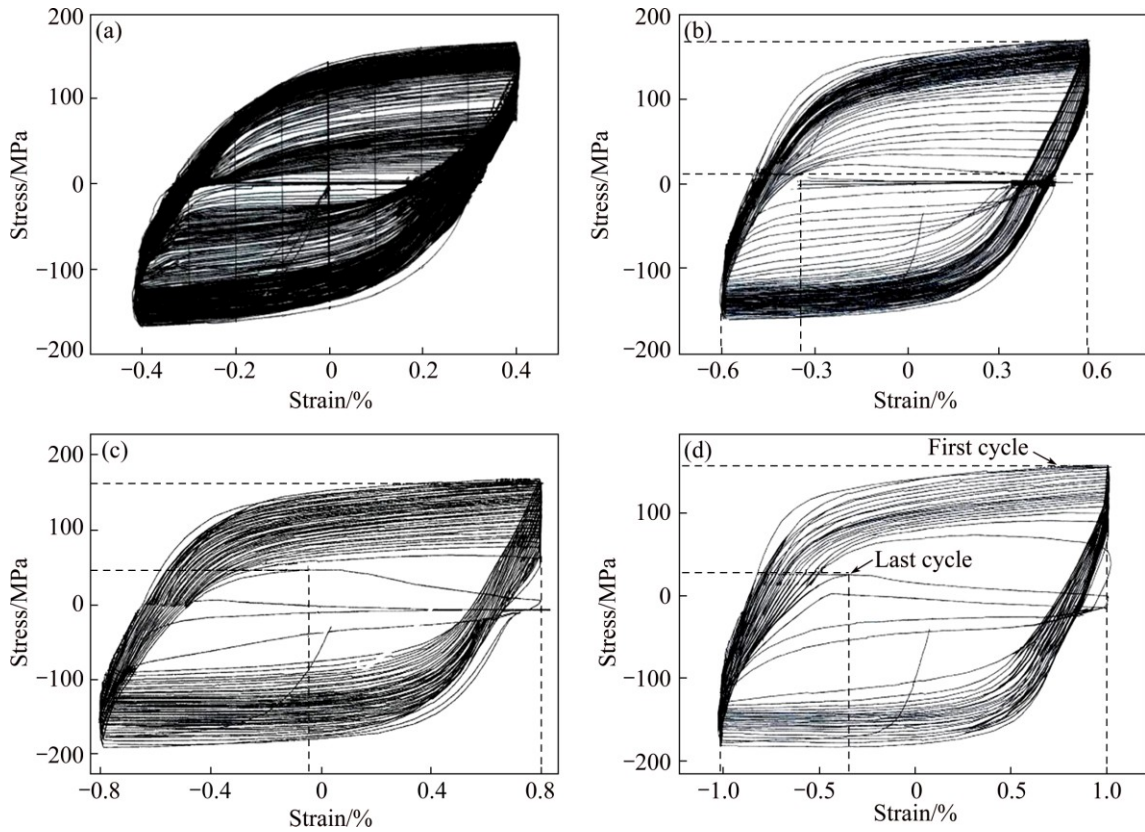


**Fig. 8** Stress–strain hysteresis loops obtained for welded specimen under LCF at  $\Delta\epsilon_t$  values of 0.8%–2%, 950 °C,  $R=-1$  and strain rate of  $3.3 \times 10^{-4} \text{ s}^{-1}$ : (a)  $\Delta\epsilon_t=0.8\%$ ; (b)  $\Delta\epsilon_t=1.2\%$ ; (c)  $\Delta\epsilon_t=1.6\%$ ; (d)  $\Delta\epsilon_t=2\%$

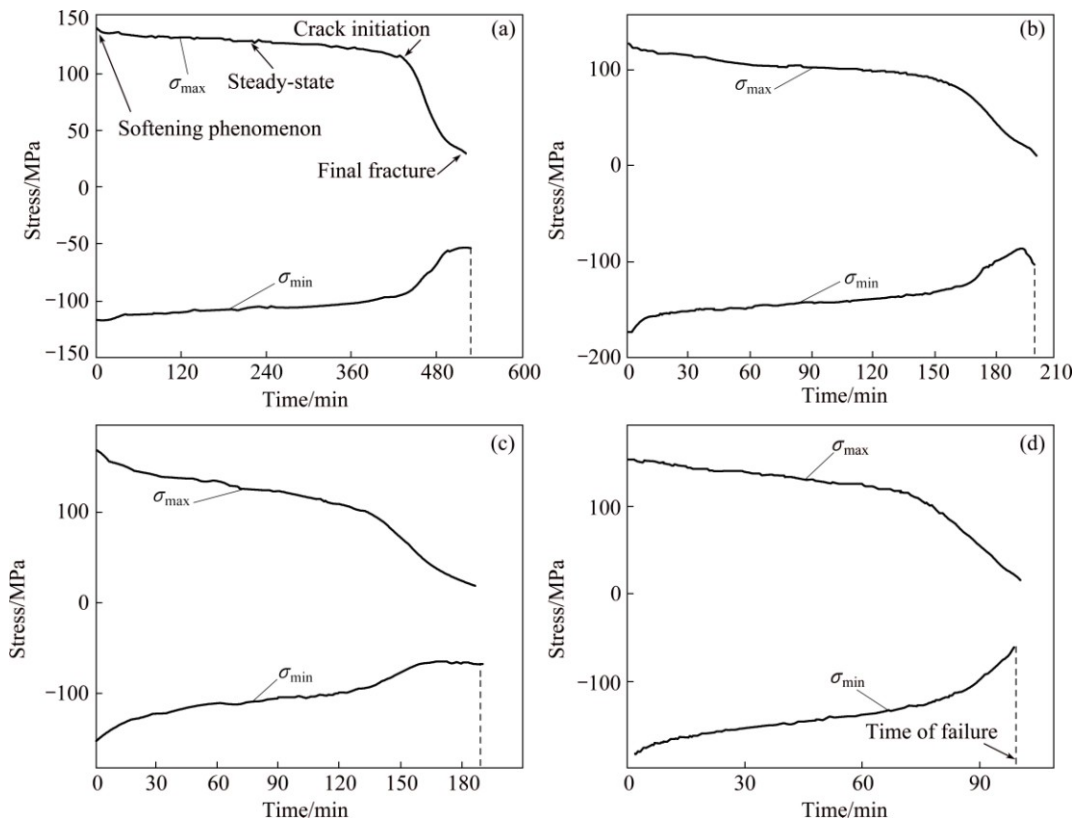


**Fig. 9** Maximum and minimum stresses versus time (cyclic softening) for unwelded specimen at  $\Delta\epsilon_t$  values of 0.8%–2%, 950 °C,  $R=-1$  and strain rate of  $3.3 \times 10^{-4} \text{ s}^{-1}$ : (a)  $\Delta\epsilon_t=0.8\%$ ; (b)  $\Delta\epsilon_t=1.2\%$ ; (c)  $\Delta\epsilon_t=1.6\%$ ; (d)  $\Delta\epsilon_t=2\%$

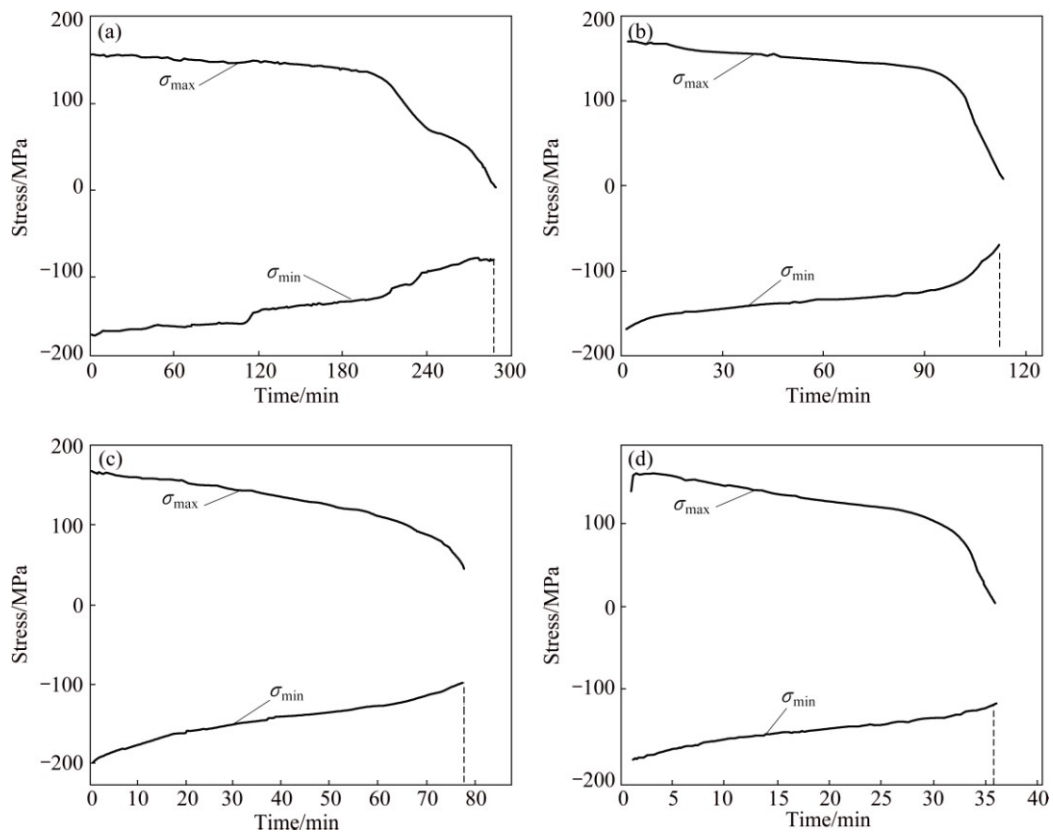


**Fig. 10** Maximum and minimum stresses versus time (cyclic softening) for welded specimen at  $\Delta\epsilon_t$  values of 0.8%–2%, 950 °C,  $R=-1$  and strain rate of  $3.3 \times 10^{-4} \text{ s}^{-1}$ : (a)  $\Delta\epsilon_t=0.8\%$ ; (b)  $\Delta\epsilon_t=1.2\%$ ; (c)  $\Delta\epsilon_t=1.6\%$ ; (d)  $\Delta\epsilon_t=2\%$

cyclic softening may be attributed to the rearrangement of dislocations, resulting from dislocation unlocking. The welded specimens are brittle and fail rapidly under conditions of applied high strain cycling at the joint interface. In this work, the softening effect was more likely caused by cracking of the carbides. The fatigue life diagram between the total strain range and the fatigue life is shown in Fig. 11. It appears that unwelded specimens showed slightly better fatigue resistance than welded specimens, especially at higher strains. Figures 12–15 show that initiation and nucleation of cracks generally start from the surface where it is always deeply oxidized. The surface grain boundary oxidation and oxide spikes are also considered as further crack nucleation sites for unwelded and welded specimens. Also, oxidation layer formed along the grain boundary. Oxide spike is formed at surface grain boundary. Depletion of Cr (due to the formation of chromium carbide phase) in the near grain boundary regions resulted in the grain boundary oxidation of Co-superalloys [27]. In welded specimens, at high cyclic strain, the nucleation and growth of cracks occurred in welded zone. But at low cyclic strain,  $\Delta\varepsilon_f=0.8\%$ , despite insufficient penetration of melts (big void), fracture occurred in the same zones of unwelded specimens (Fig. 13). Therefore, in the first stage nozzles, during the start-stop or shutdown, it is expected that the fatigue fracture will not be created in the fusion zone, if the cyclic total strain is less than 0.8%. At a high cyclic strain ( $\Delta\varepsilon_f=2\%$ ), beach marks were visible on the fracture surface of welded and unwelded specimens. Initiation of cracks generally starts from the oxidized surface grain boundary, internal voids and internal carbide interfaces. The boundary strength is degraded by oxygen diffusion. The fracture surfaces of welded and unwelded specimens at low strain cycling ( $\Delta\varepsilon_f=0.8\%$ ) show that the initiation of crack generally starts from grain boundary, internal void and internal carbide interfaces. Oxidation also

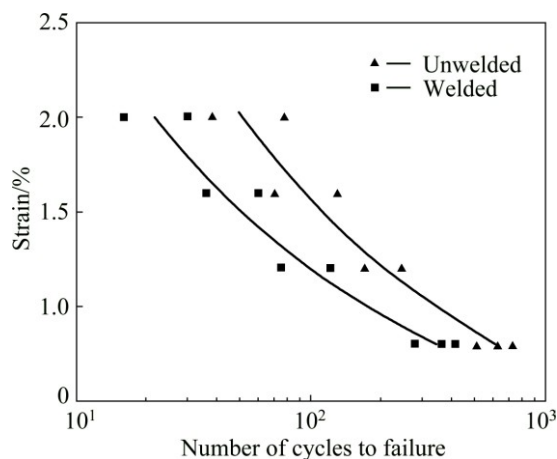


**Fig. 11** Strain–fatigue life curves for unwelded and welded specimens at 950 °C,  $R=-1$  and strain rate of  $3.3 \times 10^{-4} \text{ s}^{-1}$

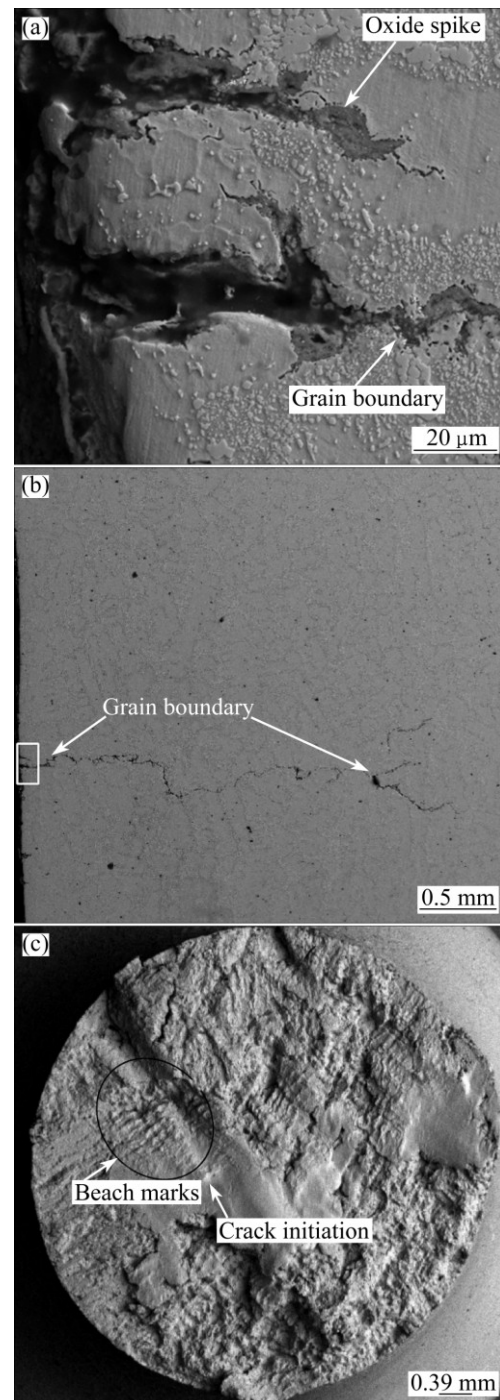


**Fig. 12** SEM images of unwelded FSX-414 specimen after LCF test at 950 °C,  $R=-1$  and  $\Delta\varepsilon_f=0.8\%$ : (a) Crack initiation from surface; (b) Crack initiation from oxide spike and grain boundary; (c) Fracture surface

accelerates fatigue damage both in terms of fatigue crack initiation and fatigue crack propagation [28]. The studies show that FSX-414 exhibits higher fatigue crack initiation and growth resistance than the weld metal, L-605 [29]. In this work, the lower fatigue life of welded specimens may be caused by the poor interfacial strength by the welding process.

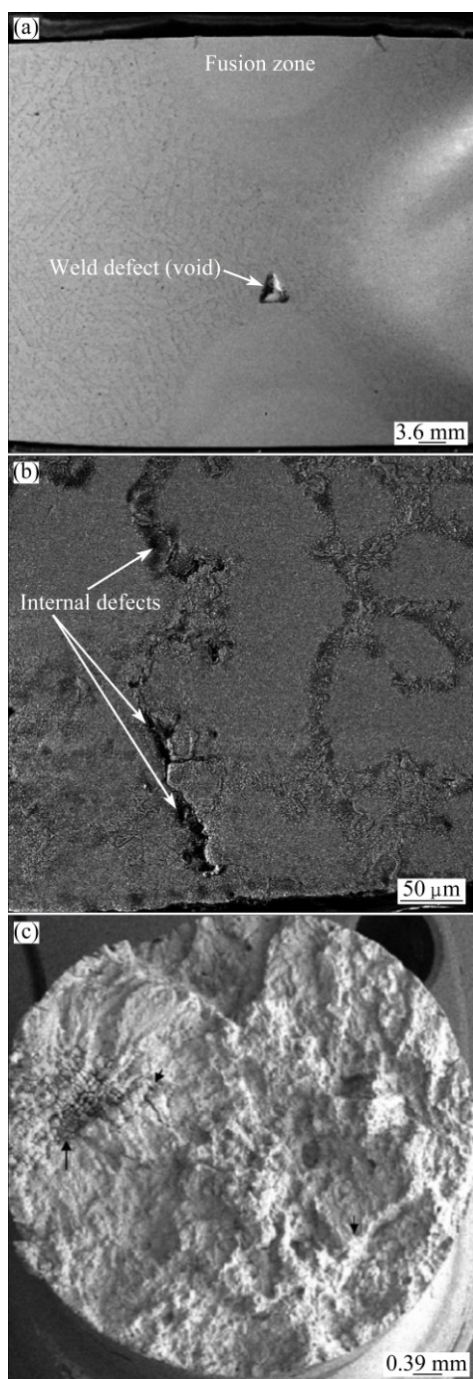


**Fig. 13** SEM images of welded FSX-414 specimen after LCF test at 950 °C and  $R=-1$  and  $\Delta\epsilon_t=0.8\%$ : (a) No cracking in welded zone; (b) Crack initiation from internal defect; (c) Fracture surface

#### 4 Conclusions

The microstructure of FSX-414 consists of  $\alpha$ -Co phase matrix, primary and secondary carbides. The weld region consists of  $\alpha$ -Cr matrix. In L-605 weld metal microstructure, there is not network carbide. Experimental tensile results show that the yield and ultimate stresses of unwelded and welded specimens are relatively equal. But toughness, reduction in area and

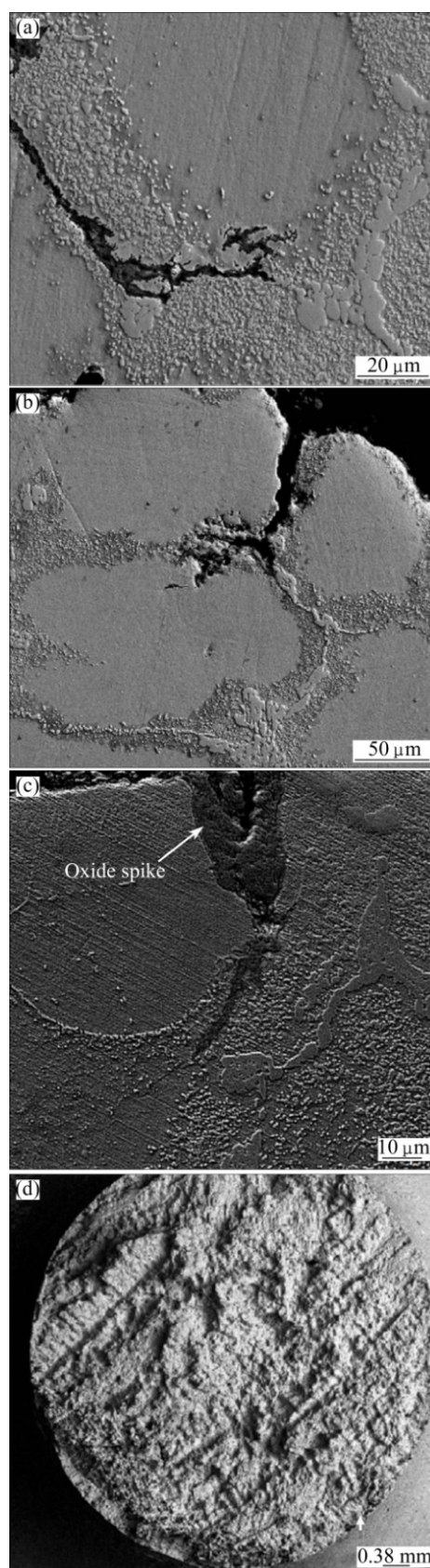


**Fig. 14** SEM images of unwelded FSX-414 specimen after LCF test at 950 °C,  $R=-1$  and  $\Delta\epsilon_t=2\%$ : (a, b) Crack initiation from grain boundary; (c) Crack initiation from oxide spike and grain boundary; (d) Fracture surface

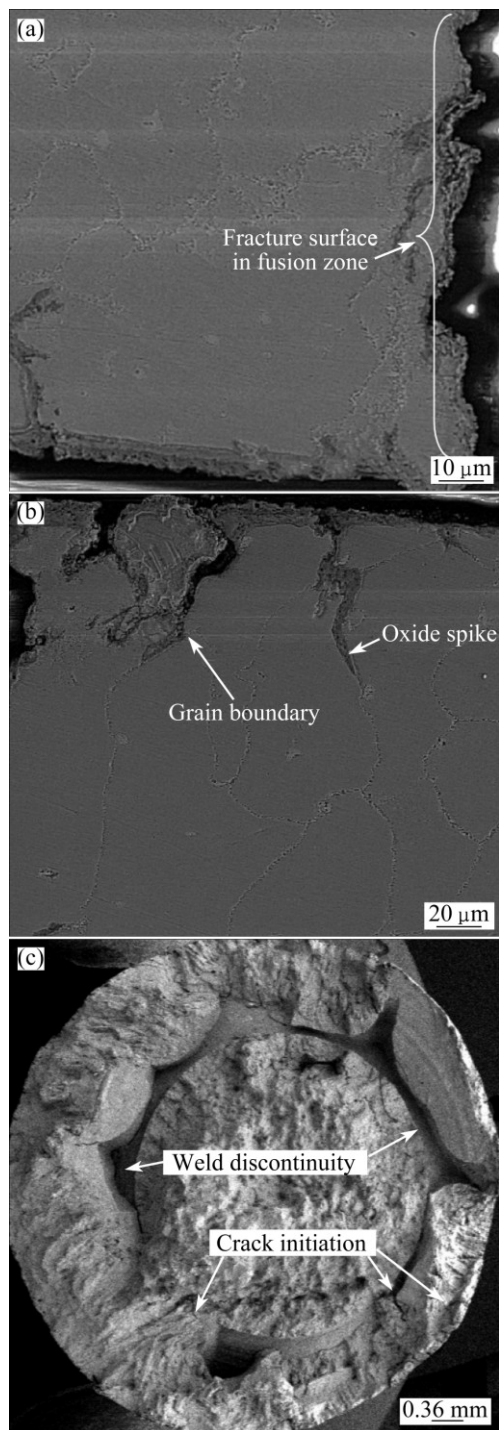


**Fig. 15** SEM images of welded FSX-414 specimen after LCF test at 950 °C,  $R=-1$  and  $\Delta\varepsilon_f=2\%$ : (a) Crack initiation from welded zone; (b) Crack initiation from oxide spike and grain boundary in fusion zone; (c) Fracture surface and weld discontinuity

elongation of welded specimens are lower than those of unwelded ones. The cleavage surfaces and big voids of the fracture surface of welded specimen due to the brittle fracture are clearly observed. Fatigue life time decreases with increasing strain amplitude. In all of the LCF tests,

softening phenomena are observed. In welded specimens, at high strain cycling, the nucleation and growth of cracks occur in the welded zone. But at  $\Delta\varepsilon_f=0.8\%$ , despite the weld discontinuity, fracture occurs in the same zones of unwelded specimens. The results of LCF tests show that L-605 alloy, as filler metal, is less resistant to LCF relative to FSX-414 alloy. Therefore, the total fatigue lives of the welded specimens are shorter than those of unwelded ones. The lower fatigue life of welded specimens may be caused by the poor interfacial strength.

### Acknowledgments

This work was supported by the Khorasan Localized Power. The authors wish to thank the Mechanical Unit Personnel of Shariati Power Plant for their assistance on this project.

### References

- [1] SCHIKE P W. Advanced gas turbine materials and coatings: Report GER-3569G general electric [R]. New York, 2004.
- [2] BALSONE S J. Bucket and nozzle [M]. Greenville: GE Company, 2004.
- [3] SIMS C T. Superalloy [M]. New York: John Wiley and Sons, 1978: 144–149.
- [4] COUSTSOURADIS D, DAVIN A. Cobalt-based superalloys for applications in gas turbines [J]. *Materials Science and Engineering A*, 1987, 88: 11–19.
- [5] MAZUR Z, HERNANDEZ-ROSSETTE A, GARCIA-ILLESCAS R, LUNA-RAMIRZA A. Failure analysis of a gas turbine nozzle [J]. *Engineering Failure Analysis*, 2008, 15: 913–921.
- [6] ZANGENEH S H, FARHANGI H. Influence of service-induced microstructural changes on the failure of a cobalt-based superalloy first stage nozzle [J]. *Materials & Design*, 2010, 31: 3504–3511.
- [7] GANDY D W, FREDERICK G, STOVER J T, VISWANATHAN R. Overview of hot section component repair methods [R]. North Charlotte: Electric Power Research Institute, Repair and Replacement Application Center, 2001.
- [8] CHASE T F, BELTRAN A M. The high-temperature properties of welded cast Co-base alloys [C]// *Proceedings of International Conference on Superalloys*. Ohio: TMS, 1972: 1–23.
- [9] DOME W A, FERRIGON S J. Brazing method helps repair aircraft gas turbine nozzles [J]. *Advanced Materials and Processes*, 1992, 3: 43–45.
- [10] SETH B B. Superalloys—The utility gas turbine perspective [C]//*Proceedings of International Conference on Superalloys*. Warrendale: TMS, 2000: 3–16.
- [11] GRANT O C, CARLL D S. Overview of transient liquid phase and partial transient liquid phase bonding [J]. *Journal of Materials Science*, 2011, 46: 5305–5323.
- [12] BAKHTIARI R, EKRAMI A. Transient liquid phase bonding of FSX-414 superalloy at the standard heat treatment condition [J]. *Materials Characterization*, 2012, 66: 38–45.
- [13] ABBASI KHAZAEI B, ASGHARI G, BAKHTIARI R. TLP bonding of dissimilar FSX-414/IN738 system with MBF80 interlayer: Prediction of solid/liquid interface location [J]. *Transactions of Nonferrous Metals Society of China*, 2014, 24(3): 996–1003.
- [14] NOWAK D G, SPIEGEL L. Shimmed laser beam welding process for joining superalloys for gas turbine applications: US Patent

- 0017906 A1 [P]. 2007–05–06.
- [15] JAHANGIRI M R, FALLAH A A. Effects of welding defects on reducing lifetimes of first stage nozzles of a 123 MW gas turbine made of FSX-414 alloy [J]. *Materials & Design*, 2011, 32: 424–432.
- [16] KISER S D. *Welding fundamentals and processes* [M]. Ohio: ASM International, 1993: 575–579.
- [17] YANG F M, SUN X F, GUANG H R, HU Z Q. On the low cycle fatigue deformation of K40S cobalt-base superalloy at elevated temperature [J]. *Materials Letters*, 2003, 57: 2823–2828.
- [18] DELPUGLIA A, BETTI F, GIORNI E, PRAESI F, ZONFRILLO G. Low-cycle and bithermal fatigue of a cobalt-base superalloy. materials for advanced power engineering [C]/Conference on Materials for Advanced Powder Engineering. Belgium, 1994: 919–928.
- [19] FUJYAMA K, OKABE N, MURAKAMI I, YOSHIOKA Y. Life assessment of high temperature low cycle fatigue of Co-base superalloy by multi-factor damage simulation analysis [J]. *Journal Society of Materials Science Japan*, 1992, 41: 1754–1759.
- [20] BICEGO V, SAMPIETRI C, TAYLOR N, GIORNI E, PINZAUTI M, GIANNOZZI M. Analysis of high temperature fatigue and creep damage for a FSX-414 gas turbine nozzle [C]/Proceedings of an International Symposium on Materials Ageing and Component Life Extension. Milan, Italy, 1995: 1085–1094.
- [21] LU Z, XU Y, HU Z. Low cycle fatigue behavior of a directionally solidified cobalt base superalloy [J]. *Materials Science and Engineering A*, 1999, 270: 162–169.
- [22] LU Y. High-temperature low-cycle-fatigue and crack-growth behaviors of three superalloys: hastelloy X, haynes 230, and haynes 188 [D]. Knoxville: University of Tennessee, 2005.
- [23] MIGLIETTI W, KEARNEY J, PABON L. Liquid phase diffusion bond repair of siemens V84.2, row 2 vanes and Alstom Tornado, 2nd stage stator segments. ASME 2001–GT–0510 [R]. New Orleans, Louisiana: ASME, 2001.
- [24] MIGLIETTI W, RODRICK J. Extending useful life of a cobalt-based gas turbine component: US Patent, 0084980A1 [P]. 2012–07–18.
- [25] MIGLIETTI W. Wide gap diffusion braze repairs of nozzle segments cast from FSX-414 Co-based superalloy, brazing and soldering [C]/Proceedings of the 3rd International Brazing and Soldering Conference. San Antonio, Texas, USA, 2006.
- [26] RAHMANI Kh. Research on failure of GE-F9 gas turbine vanes and life assessment after repairing: Report MCH-1484-83 [R]. Tehran: Shahid Beheshti University, 2009.
- [27] HOU G, LIU Z, WEI H, ZHENG Q, SUN X, GUAN H, HU Z. Oxidation of Co-base superalloy [J]. *Journal of Material Science and Technology*, 2008, 24: 883–890.
- [28] LIU H W, OSHIDA Y. Literature survey on oxidations and fatigue lives at elevated temperatures: NASA Contractor Report 174639 [R]. New York, 1984.
- [29] PALLOS K J. Gas turbine repair technology [M]. Atlanta: GE Energy Services Technology, 2001.

## 焊接工艺对 FSX-414 钴基高温合金低周疲劳性能的影响

Kh. RAHMANI, A. TORABIAN

Energy and Mechanical Engineering Department, Abbaspour College of Engineering,  
Shahid Beheshti University, P. O. Box16765-1719, Tehran, Iran

**摘要:** FSX-414 钴基高温合金已应用于制造燃气轮机一级喷嘴, 当燃气轮机运行时, 其第一级喷嘴处于低周疲劳状态, 这样的作业条件使喷嘴等部件开裂。通常选用钴基合金采用钨极电弧焊接(TIG)技术对喷嘴上的裂纹进行焊接。研究 TIG 对 FSX-414 钴基高温合金在 950 °C 时拉伸及低周疲劳性能的影响。在应变速率为  $3.3 \times 10^{-4} \text{ s}^{-1}$ 、应变率  $R$  为  $-1 (R = \epsilon_{\min} / \epsilon_{\max})$ 、总应变变化值  $\Delta \epsilon_i$  为 0.8%~2% 的条件下研究 FSX-414 合金的低周疲劳性能。实验结果表明: 焊接和非焊接样品的屈服应力和最大拉伸应力相近, 但焊接样品的韧性比非焊接样品的低。对于焊接试样, 在高应变条件下, 焊缝区发生裂纹的成核和扩展。但当  $\Delta \epsilon_i = 0.8\%$  时, 在非焊接试样的相同区域发生断裂。上述结果表明, 焊接试样的总疲劳寿命低于非焊接试样的总疲劳寿命。此外, 在所进行的低周疲劳实验中均观察到了软化现象。

**关键词:** 钴基高温合金; 拉伸性能; 低周疲劳; 焊接

(Edited by Wei-ping CHEN)